Hindawi
Adsorption Science & Technology
Volume 2021, Article ID 4556493, 15 pages
https://doi.org/10.1155/2021/4556493

Research Article

Electron-Scale Insights into the Single and Coadsorption Cd(II) Behaviors of a Metal-Nonmetal-Modified Titanium Dioxide

Jingjing Ren,[1] Liuchun Zheng,[1,2] Feixiong Yang,[1] Huajian Yu,[1] Tao Zhang,[1] Qianya Zhou,[1] Hao Zeng,[1] Lijuan Zhang,[3] and Peipei Meng[4]

[1]*School of Environment, South China Normal University, Guangzhou Higher Education Mega Center, Guangzhou 510006, China*
[2]*Guangdong Provincial Key Laboratory of Chemical Pollution and Environmental Safety & MOE Key Laboratory of Theoretical Chemistry of Environment, South China Normal University, Guangzhou 510006, China*
[3]*School of Chemistry and Chemical Engineering, South China University of Technology, Guangzhou 510640, China*
[4]*College of Environment, Jinan University, Guangzhou 510632, China*

Correspondence should be addressed to Liuchun Zheng; lczhengscnu1@163.com

Received 9 July 2021; Accepted 6 October 2021; Published 29 October 2021

Academic Editor: Rangabhashiyam Selvasembian

Metal (Fe) and nonmetal (P) were used to modify TiO_2, and then, several functional groups such as P-O, P=O, Fe-O, and -OH were introduced on its surface to enhance the adsorption capacity for Cd(II), which could reach 121 mg/g. According to the experimental analysis of adsorption performance, chemical adsorption dominates the adsorption process, and the adsorption capacity increases with increasing temperature within a certain range. The results of competitive adsorption experiments showed that both Pb(II) and Cu(II) affect the adsorption of Cd(II) and that the adsorption order of P-Fe-TiO_2 for heavy metal ions is Pb(II) > Cd(II) > Cu(II). We further investigated the adsorption mechanism of P-Fe-TiO_2 for Cd(II) and the reasons for the difference in competitive adsorption and used DFT calculations to confirm the experimental results. In the analysis of binding energy and frontier molecular orbitals (FMOs), we confirmed that charge transfer occurred during the adsorption process, so chemical reactions occurred. The binding energy of P-Fe-TiO_2 and Pb(II) is the largest. The results of the competitive adsorption experiment also confirmed that the adsorbent has the greatest effect on Pb. Mulliken analysis was used to identify the best binding site on the adsorbent. The results of electrostatic potential, total potential, and differential charge analysis further prove the conclusions described above.

1. Introduction

Water pollution by heavy metals is a serious environmental problem endangering human health [1–3]. At present, wastewater from many industries, such as the metallurgical, mining, chemical, and manufacturing industries, contains a variety of toxic heavy metal ions. Among these ions, cadmium (Cd) causes the most serious pollution [4]. Cd is easily enriched in organisms and is difficult to degrade. Long-term exposure to excessive amounts of Cd can cause damage to the human kidney and liver and may even cause carcinogenic and teratogenic lesions [5]. For this reason, various high-efficiency water treatment technologies, such as chemical precipitation, ion exchange, flotation, membrane filtration [6], electrochemical treatment [7], coagulation-flocculation, and adsorption, are used to remove Cd(II) [8]. Compared with other methods, the adsorption method has the advantages of high efficiency, excellent performance, easy operation, low cost, and environmental friendliness [9].

In the adsorption method, the choice of adsorbent is particularly important. In recent years, TiO_2 nanomaterials have been used in the field of sewage treatment because of their environmental friendliness, high stability, and low price [10, 11]. Although TiO_2 has been widely used in photocatalytic materials, it also has great potential for use in adsorption. Researchers have successfully prepared a variety of high-specific-surface-area nano-TiO_2 materials for the adsorption of heavy metal ions [12–14]. Wu et al. [15] used the hard template method to prepare bean-shaped TiO_2 with a maximum adsorption capacity of 10 mg/g for heavy

metals. Wang et al. [16] prepared TiO_2 nanotubes with a maximum adsorption capacity of 50.95 mg/g. Liu et al. [17] prepared TiO_2 nanotubes containing a large amount of hydroxyl groups with a maximum adsorption capacity of 67 mg/g. The specific surface area and functional groups are two important factors that can affect the adsorption capacity of TiO_2. Therefore, it is necessary to synthesize TiO_2 adsorption materials with a high specific surface area and rich functional groups. In a previous study, Zhang et al. [18] prepared Fe-doped TiO_2 metal oxide materials to remove Cu(II) in wastewater, and the adsorption removal rate was as high as 88.54%. Peng et al. [19] prepared phosphoric acid-modified TiO_2, a nonmetal oxide adsorbent, with an adsorption capacity of 92 mg/g for Cr (III). The modification of TiO_2 with metal oxides and nonmetal oxides can introduce functional groups and increase its specific surface area, increasing the adsorption capacity, but the adsorption and removal of heavy metal ions by TiO_2 modified by loading with a single metal or nonmetal are still limited, so we used a combination of a metal and nonmetal to modify TiO_2 and investigated the adsorption performance of the resulting material. In this study, potassium dihydrogen phosphate and ferric chloride were used to modify TiO_2. The resulting adsorbent has good adsorption capacity for Cd(II), Pb(II), and Cu(II). The adsorption behavior was also confirmed by DFT calculations.

2. Materials and Methods

2.1. Materials and Chemicals. Raw TiO_2 was purchased from a company in Guangzhou, China. All chemicals (analytical reagent grade) were purchased from Chemical Reagent Co., Ltd. (Guangzhou, China) and were employed without any further purification. The required concentration of Cd(II) aqueous solution was prepared by mixing an appropriate quantity of cadmium nitrate tetrahydrate crystals and deionized water. The initial pH of each solution was adjusted by the addition of diluted HNO_3 or NaOH solution.

2.2. Preparation. Initially, 0.8 mol·L^{-1} KH_2PO_4 and 1.5 mol·L^{-1} $FeCl_3$ solutions were prepared for later use. Second, 10 g raw TiO_2 was weighed into a beaker, 140 mL of prepared KH_2PO_4 solution and 100 mL of $FeCl_3$ solution were added, and the mixture was stirred at 25°C for 1 h. Afterwards, the pH of the solution was adjusted to approximately 9.5, and the solution was aged for 2 h. The solution was subjected to suction filtration until no excess water was present, rinsed with deionized water three to five times, washed until the material was neutral, filtered, dried, and ground through a 100-mesh sieve. The resulting material was denoted as P-Fe-TiO_2 and stored in a vacuum-sealed bag.

2.3. Characterization. Scanning electron microscopy (SEM, Hitachi S-3400N, Japan) and energy-dispersive spectrometry (EDS, INCA ENERGY 350, UK) were used to observe the microscopic surface morphology of the TiO_2 materials and determine the element content. The specific surface area, average pore size, and total pore volume were measured using BET (Micromeritics ASAP 2460, USA). FTIR spectra of the materials were obtained in the wavenumber range from 600 to 4000 cm^{-1} on a Fourier transform infrared (FTIR) spectrophotometer (Thermo Nicolet 6700, USA) with the KBr pellet technique at room temperature. X-ray photoelectron spectroscopy (XPS, Thermo Scientific ESCALAB 250Xi, USA) was used to determine the element composition and peak valence states of the sample surface and other information. The XPS data were collected with a monochromatic Al K alpha source operated at 230 W and fitted using XPSPEAK software. X-ray diffractometry (XRD) was performed from 10 to 80° on an X-ray diffractometer (D/max-IIIA, Rigaku, Japan) with filtered Cu Kα radiation generated at 45 kV and 40 mA.

2.4. Cd(II) Adsorption Study. $Cd(NO_3)_2{\cdot}4H_2O$ crystals and deionized water were used to prepare a Cd(II) solution with a concentration of 100 mg/L. To determine the optimal pH, 0.02 g of TiO_2 and P-Fe-TiO_2 were weighed into a 10 mL Erlenmeyer flask, Cd(II) solution adjusted to pH 2, 4, 5, 6, or 8 was added, and the mixture was shaken at 25°C for 3 h. Under the above conditions, 10°C, 25°C, and 40°C were selected for the adsorption process. Single and composite mixed solutions of 0, 20, 50, and 100 mg/L Pb(II) and Cu(II) were prepared in 100 mg/L Cd(II) solution. The other experimental conditions were the same as above, and heavy metal competitive adsorption experiments were carried out. Finally, atomic absorption spectroscopy (Model AA7000, Shimadzu, Japan) was used to determine the concentration of heavy metal ions in the solution after adsorption equilibrium. Three parallel samples were set for each sample. The calculation equations for the adsorption rate (A) and adsorption capacity (q_t) are as follows:

$$A = \frac{C_0 - C_t}{C_0} \times 100\%, \quad (1)$$

$$q_t = \frac{(C_0 - C_t) \times V}{M}. \quad (2)$$

C_0 is the concentration of heavy metal ions in the initial solution (mg/L), C_t is the concentration of heavy metal ions in the filtrate after adsorption for a certain period of time (mg/L), V is the volume of the solution (L), and M is the adsorbent dosage (g).

Under the abovementioned optimal conditions, 250 mL and 400 mg/L Cd(II) solutions were prepared, and 0.5 g of the P-Fe-TiO_2 or TiO_2 material was weighed into a 250 mL Erlenmeyer flask and oscillated at 10, 25, and 40°C. The materials were treated for 3 hours at a speed of 180 r·min^{-1}, and samples were taken at different time points, after which the amount of heavy metal adsorption was calculated according to equation (2). The experimental results were fitted with a pseudo-first-order kinetic model and a pseudo-second-order kinetic model.

The pseudo-first-order kinetic model is based on the assumption that the adsorption process is mainly affected by the diffusion step, and the expression is shown in equation (3)[20]

$$\log (q_e - q_t) = \log q_e - \frac{K_f}{2.303} t. \quad (3)$$

The pseudo-second-order kinetic model assumes that the square of the number of vacancies not occupied by the adsorbent on the surface of the adsorbent determines the adsorption rate, and the expression is shown in equation (4)[21]

$$\frac{t}{q_t} = \frac{1}{K_2 q_e^2} + \frac{t}{q_e}. \quad (4)$$

q_e is the amount of adsorption at adsorption equilibrium (mg/g), q_t is the amount of adsorption at time t (mg/g), K_f is the pseudo-first-order rate constant, and K_2 is the pseudo-second-order rate constant.

Cd(II) solutions with concentrations of 10, 50, 100, 200, 300, and 500 mg/L were prepared. A total of 0.02 g P-Fe-TiO_2 or TiO_2 was added to an Erlenmeyer flask, and different concentrations of Cd(II) solution were added; the other reaction conditions were the same as above. The adsorption capacity was calculated according to equation (1), and the Langmuir and Freundlich adsorption isotherm models were fitted to the experimental results, as shown in equations (5) and (6), respectively [22].

$$\frac{C_e}{q_e} = \frac{C_e}{q_m} + \frac{1}{K_L q_m}, \quad (5)$$

$$\log q_e = \frac{\log C_e}{n} + \log K_F, \quad (6)$$

where c_e is the adsorption equilibrium concentration of metal ions in the solution (mg/L), K_L is the Langmuir constant (L/mg), q_m is the saturated adsorption capacity, $1/n$ is the adsorption strength, and K_F is the Freundlich constant (L/mg).

The Gibbs free energy (ΔG), enthalpy (ΔH), and entropy (ΔS) can be calculated from equations (7), (8) (9) and (10) [23]

$$K_D = \frac{q_e}{c_e}, \quad (7)$$

$$\Delta G = -RT \ln K_D, \quad (8)$$

$$\Delta G = \Delta H - T\Delta S, \quad (9)$$

$$\ln K_D = \frac{\Delta S}{R} - \frac{\Delta H}{RT}, \quad (10)$$

where T is temperature (K) and K_D is the distribution coefficient ($mL\,g^{-1}$). The enthalpy change (ΔH) and the entropy (ΔS) can be calculated from a plot of $\ln K_D$ versus $1/T$.

2.5. DFT Calculations. The adsorption mechanism of P-Fe-TiO_2 on Cd(II) can be simulated by spin-polarized density functional theory (DFT). The Dmol3 software package in Materials Studio 2017 R2 was used to perform quantum molecule (QM), molecular orbital (MO), and Mulliken and binding energy analysis with quantum chemical calculation methods based on the first principles and DFT. The atomic center grid was used for atomic basis functions, the electron basis set was dual numerical polarization (DNP 3.5), and all electron methods were used as core processing methods. Both the generalized gradient correction (GGA) and Perdew-Burke-Ernzerhof (PBE) functions were used to describe electron exchange interactions. A conductor-like shield model (COSMO) with a dielectric constant of 78.54 (water) was used in the simulation. To make the fitting more accurate, the tolerances of energy, force, and displacement were set to 1.0×10^{-5} Ha, $2 \times 10 - 3$ Ha $Å^{-1}$, and 5×10^{-3} Å, respectively. In addition, the adsorption binding energy on P-Fe-TiO_2 was calculated according to Equation (11).

$$E = E_{(ab)} - E_{(a)} - E_{(b)}, \quad (11)$$

where $E_{(ab)}$ is the total adsorption binding energy of the adsorption complex and $E_{(a)}$ and $E_{(b)}$ are the total energy of the adsorbent and the adsorbate, respectively. The greater the absolute value of E is, the stronger the binding between the adsorbate and the adsorbent.

3. Results and Discussion

3.1. SEM-EDS and BET Analysis. As shown in Figure 1, TiO_2 has more surface impurities than P-Fe-TiO_2, which may block adsorption pores. In contrast, the structure of P-Fe-TiO_2 is fluffier, and the surface of the material is loaded with many particles, which increases its specific surface area; this particle loading indicates that phosphoric acid groups were successfully loaded on the surface of TiO_2. The surface roughness of the adsorbed P-Fe-TiO_2-Cd was obviously reduced, which proves that the adsorption process proceeded smoothly [24]. As expected, the Brunauer-Emmett-Teller (BET) characterization results showed that the specific surface area, average pore size, and total pore volume were 51.66 m^2/g, 15.7 nm, and 0.0021 cm^3/g for TiO_2 and 54.19 m^2/g, 8.73 nm, and 0.0037 cm^3/g for P-Fe-TiO_2. P-Fe-TiO_2 thus provides a larger contact area to promote physical adsorption. In addition, the EDS analysis results showed that the P content increased from 0% to 9.35% after modification and the content of Cd increased from 0% to 11.71% after adsorption, which means that phosphorus-containing groups were successfully loaded onto the TiO_2 surface and that P-Fe-TiO_2 has a good adsorption effect for Cd(II). Compared with the Fe content of TiO_2, the Fe content of P-Fe-TiO_2 also increased significantly, indicating that iron was also successfully loaded on the surface of TiO_2, providing the modified material with magnetic properties.

3.2. FTIR and XRD Analysis. The FTIR characterization results of TiO_2, P-Fe-TiO_2, and P-Fe-TiO_2-Cd are shown in Figure 2(a). The three materials all have a -OH group stretching vibration peak at 3396 cm^{-1} and a -OH group characteristic peak at 1630 cm^{-1} [25]. The peak at 400~800 cm^{-1} is the characteristic peak of Ti-O-Ti stretching

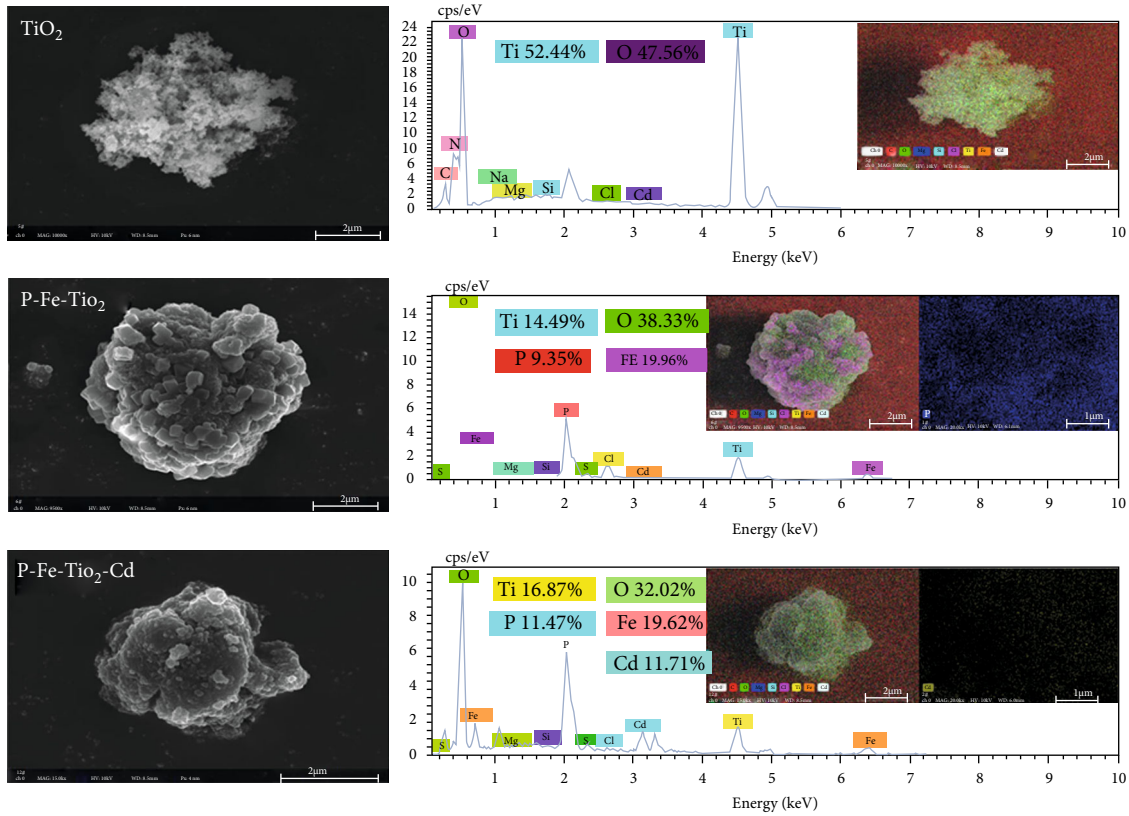

Figure 1: SEM images and EDS spectra of TiO_2, P-Fe-TiO_2, and P-Fe-TiO_2-Cd with EDS elemental distribution mapping images of P for P-TiO_2 and Cd for P-TiO_2-Cd.

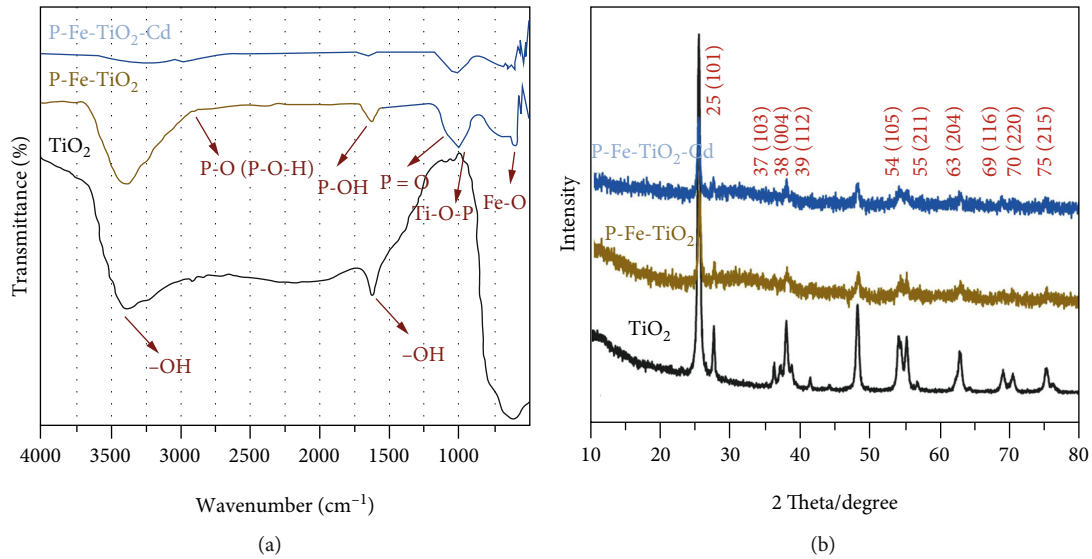

Figure 2: (a) FTIR spectra and (b) XRD patterns of TiO_2, P-Fe-TiO_2, and P-Fe-TiO_2-Cd.

vibrations [26]. In P-Fe-TiO_2, the characteristic peak of νP-O in P-O-H appeared near 2890 cm^{-1} [27]. In addition, new characteristic peaks appeared at 900-1700 cm^{-1}, confirming the presence of phosphorus-containing groups. For example, the band at 1640 cm^{-1} was attributed to δP-OH [28]. In the modified material, the characteristic peak appearing near 1035 cm^{-1} is the stretching vibration peak of Ti-O-P [29]. This result shows that potassium dihydrogen phosphate and titanium dioxide are connected by O atoms, which confirms the introduction of P-O functional groups. In addition, the characteristic peak of P=O appeared at 1080 cm^{-1} [30]. However, there is no characteristic peak between 700 and 800 cm^{-1}, so there are no P-P bonds in P-Fe-TiO_2. The characteristic peak of Fe-O appeared at 588 cm^{-1}, indicating that

Fe was successfully loaded on P-Fe-TiO_2 [31]. This result shows that iron trichloride and titanium dioxide are connected by O atoms, confirming the introduction of Fe-O functional groups. The results of XRD characterization analysis are shown in Figure 2(b). The XRD diffraction patterns of TiO_2, P-Fe-TiO_2, and P-Fe-TiO_2-Cd all match the corresponding standard card (JCPDS No. 21-1272), and there are no obvious impurity peaks, indicating that the structure is anatase TiO_2 [32]. The intensities of the XRD diffraction peaks of P-Fe-TiO_2 and P-Fe-TiO_2-Cd are weaker than those of TiO_2, indicating that the introduction of phosphorus-containing groups reduced the crystallinity of TiO_2 [33].

3.3. XPS Analysis. The XPS spectra of P-Fe-TiO_2 and P-Fe-TiO_2-Cd are shown in Figure 3. In the total spectrum (Figure 3(a)), P-Fe-TiO_2-Cd has characteristic Cd peaks (Figure 3(b)) at 405.35 eV ($Cd_{5/2}$) and 412.09 eV ($Cd_{3/2}$), indicating that P-Fe-TiO_2 can successfully adsorb Cd(II). Moreover, the characteristic peak of P 2p appeared near 133 eV, indicating that P exists in the pentavalent state (P^{5+}) in P-Fe-TiO_2 and P-Fe-TiO_2-Cd (Peng and Du et al., 2020). However, there is no peak for P at a binding energy of 218.16 eV, so there are no Ti-P bonds in P-Fe-TiO_2 [34]. The Fe 2p pattern of P-Fe-TiO_2 is mainly composed of Fe $2p_{3/2}$ and Fe $2p_{1/2}$, as shown in Figures 3(c) and 3(d). The peak near 711 eV in Fe $2p_{3/2}$ belongs to Fe-OH or Fe-O, which adsorb Cd(II), and the characteristic peak positions of Fe-OH and Fe-O of P-Fe-TiO_2-Cd changed after adsorption [35]. After adsorption, the peak positions and areas of P $2p_{3/2}$ and P $2p_{1/2}$ of P-Fe-TiO_2-Cd changed accordingly (Figures 3(e) and 3(f)), which indicates that the addition of phosphorus-containing groups is beneficial to the complexation of Cd [36].

3.4. Effects of pH Value and Coexisting Heavy Metal Ions and Adsorption Isotherms. The pH value of the solution will affect the charge and stability of the functional groups on the surface of an adsorbent material, thereby affecting its adsorption performance [37]. As shown in Figure 4(a), when the pH is 2.0, the two materials basically have no adsorption effect. This is because in an acidic environment, a large amount of H^+ will generate H_3O^+ and bind to the surface of the adsorbent, leading to the protonation of adsorption sites; furthermore, the surface is positively charged, so Cd(II) cannot closely approach the adsorption site due to electrostatic repulsion and therefore cannot undergo adsorption. With increasing pH, the adsorption capacity of P-Fe-TiO_2 on Cd(II) first increased, tended towards equilibrium, and then decreased, and a pH greater than 4 was conducive to the adsorption of Cd(II), which was similar to the experimental conclusions of Yao et al. [38]. This trend was observed because an appropriate amount of -OH groups can promote an increase in adsorption capacity. Some Cd(II) combines with OH^- to form $Cd(OH)^+$. On the one hand, $Cd(OH)^+$ formation will reduce the charge on the surface of the material and weaken electrostatic repulsion; on the other hand, $Cd(OH)^+$ helps to improve the binding capacity of the adsorption sites for Cd(II) [39]. However, when the pH of the solution reaches 8.0, a large amount of $Cd(OH)^+$ is produced and continues to form $Cd(OH)_2$ precipitation with OH^-, so the adsorption capacity will decrease. Since a certain amount of -OH can promote the adsorption process, 6.0 was used as the solution pH for the remaining adsorption experiments. As shown in Figures 4(b) and 4(c) and Table 1, the Freundlich and Langmuir adsorption isotherm models were used to fit the adsorption behavior of TiO_2 and P-Fe-TiO_2 for Cd(II). The experimental data fit more closely to the Langmuir equation, and the correlation $R^2 > 0.98$. Therefore, the adsorption of Cd(II) by P-Fe-TiO_2 involves typical monolayer adsorption [40]. According to the fitting results, the theoretical maximum adsorption capacity of P-Fe-TiO_2 reached 83.3 mg/g. Moreover, the adsorption capacity of P-Fe-TiO_2 is significantly higher than that of some existing TiO_2 materials, such as TiO_2 beads (10 mg/g) [15], TiO_2 nanotubes (50.95 mg/g) [15], and mesoporous phosphated TiO_2 (92 mg/g) [19]. The competitive adsorption of Pb(II) and Cu(II) single metals and composite metals with Cd(II) is shown in Figures 4(d)–4(f). From the figure, as the concentration of competing metal ions increases, the adsorption capacity of P-Fe-TiO_2 for Cd(II) gradually decreases, and the adsorption capacity for Pb(II) and Cu(II) gradually increases. Overall, the adsorption capacity follows the order $Pb(II) > Cd(II) > Cu(II)$. This order corresponds to the radii of the metal ions and their electronegativity [41]. Compared with Cd (1.69) and Cu (0.73), Pb has greater electronegativity (2.33) [42], and the ionic radius of Pb (1.2 Å) is larger than that of Cd (0.95 Å) but smaller than that of Cu (1.9 Å) [43]. Therefore, it is speculated that electronegativity is the most important factor affecting the competitive adsorption process.

3.5. Adsorption Kinetics. The adsorption kinetics data of P-Fe-TiO_2 and TiO_2 at the initial concentration of 100 mg/L and 400 mg/L were fitted with the pseudo-first-order kinetic model and pseudo-second-order kinetic model, and the fitting results are shown in Figure 5 and Table 2. The fitting results of the experimental data are consistent with the pseudo-first-order kinetic model and pseudo-second-order kinetic model, indicating that chemical adsorption and physical adsorption are the rate control steps of P-Fe-TiO_2 adsorption of Cd(II) [44]. The reason for physical adsorption is the increase with the surface area of the adsorbent after modification, and the introduction of functional groups is the reason for chemical adsorption. As the temperature increases, the adsorption capacity of P-Fe-TiO_2 gradually increases, indicating that increasing the temperature helps to improve the adsorption performance. TiO_2 and phosphoric acid groups will stack into a disordered network structure of -P-O-Ti-O-, and this structure will undergo a certain degree of hydrolysis in aqueous solution [19] and introduce P-O functional group modification at the same time. In the same way, modification with $FeCl_3$ will introduce Fe-O functional groups into the modified material (Zhang and [18]). The introduction of functional groups was confirmed in the FTIR analysis; these functional groups can promote chemical adsorption. The increase of the specific surface area is conducive to the occurrence of physical adsorption and

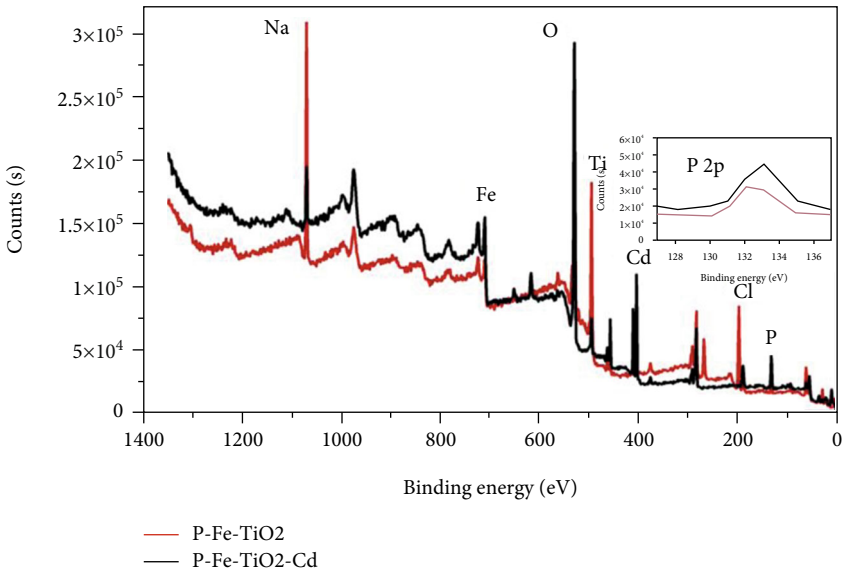

(a)

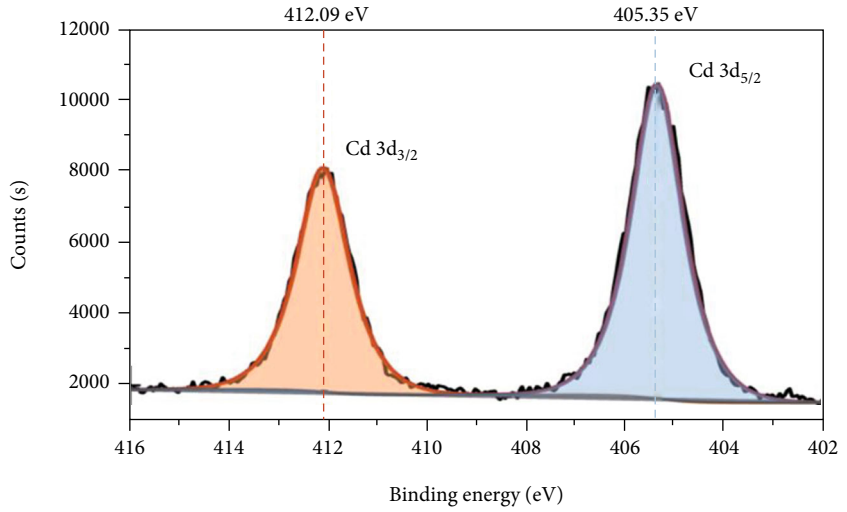

(b)

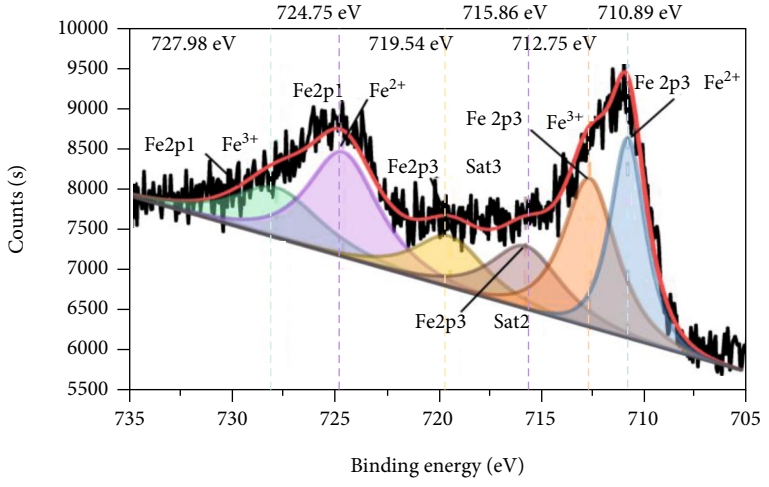

(c)

Figure 3: Continued.

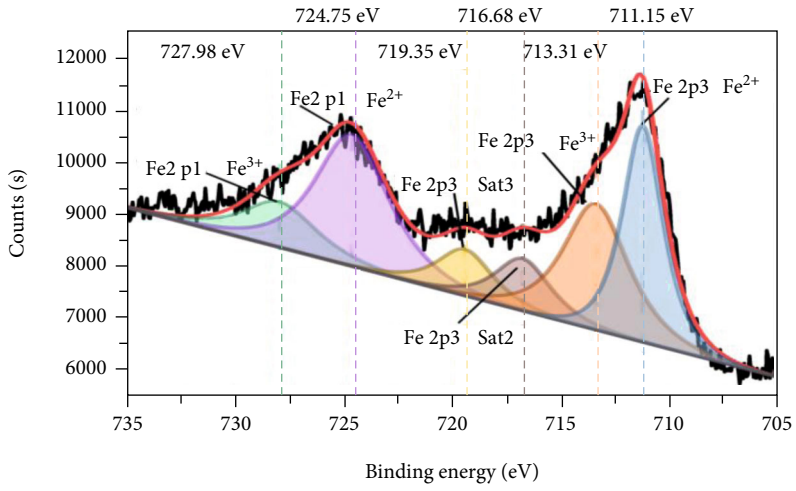

(d)

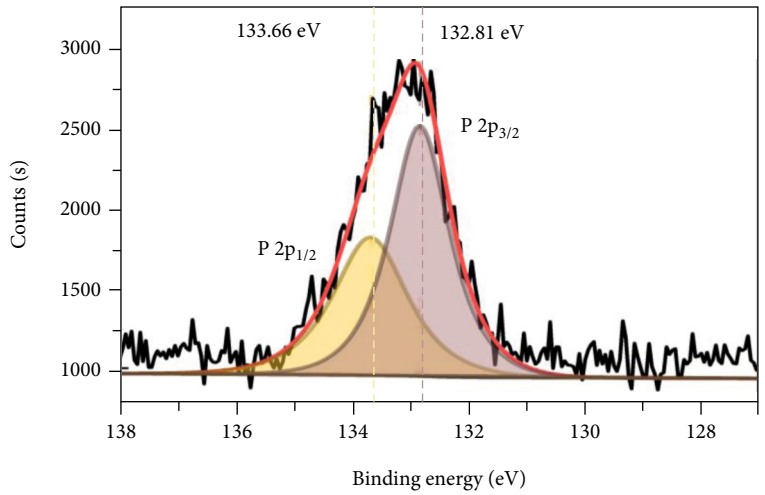

(e)

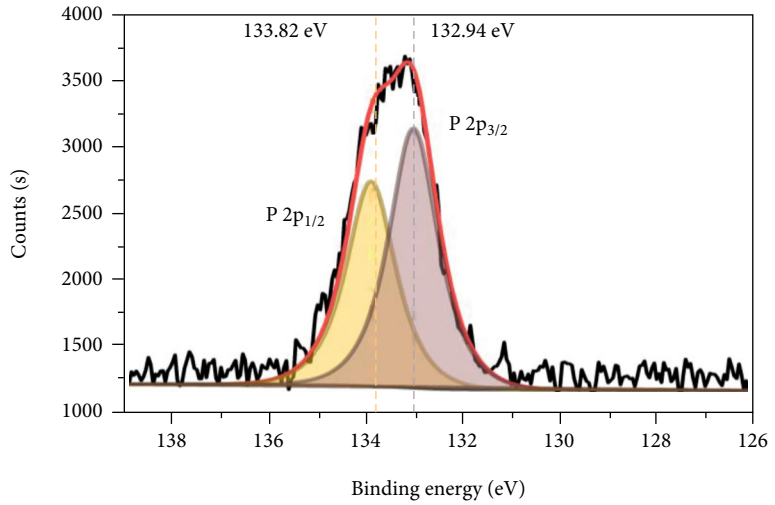

(f)

Figure 3: XPS spectra of P-Fe-TiO_2 and P-Fe-TiO_2-Cd: (a) wide scan, (b) Cd 3d, (c) Fe 2p of P-Fe-TiO_2, (d) Fe 2p of P-Fe-TiO_2-Cd, (e) P 2p of P-Fe-TiO_2, and (f) P 2p of P-Fe-TiO_2-Cd.

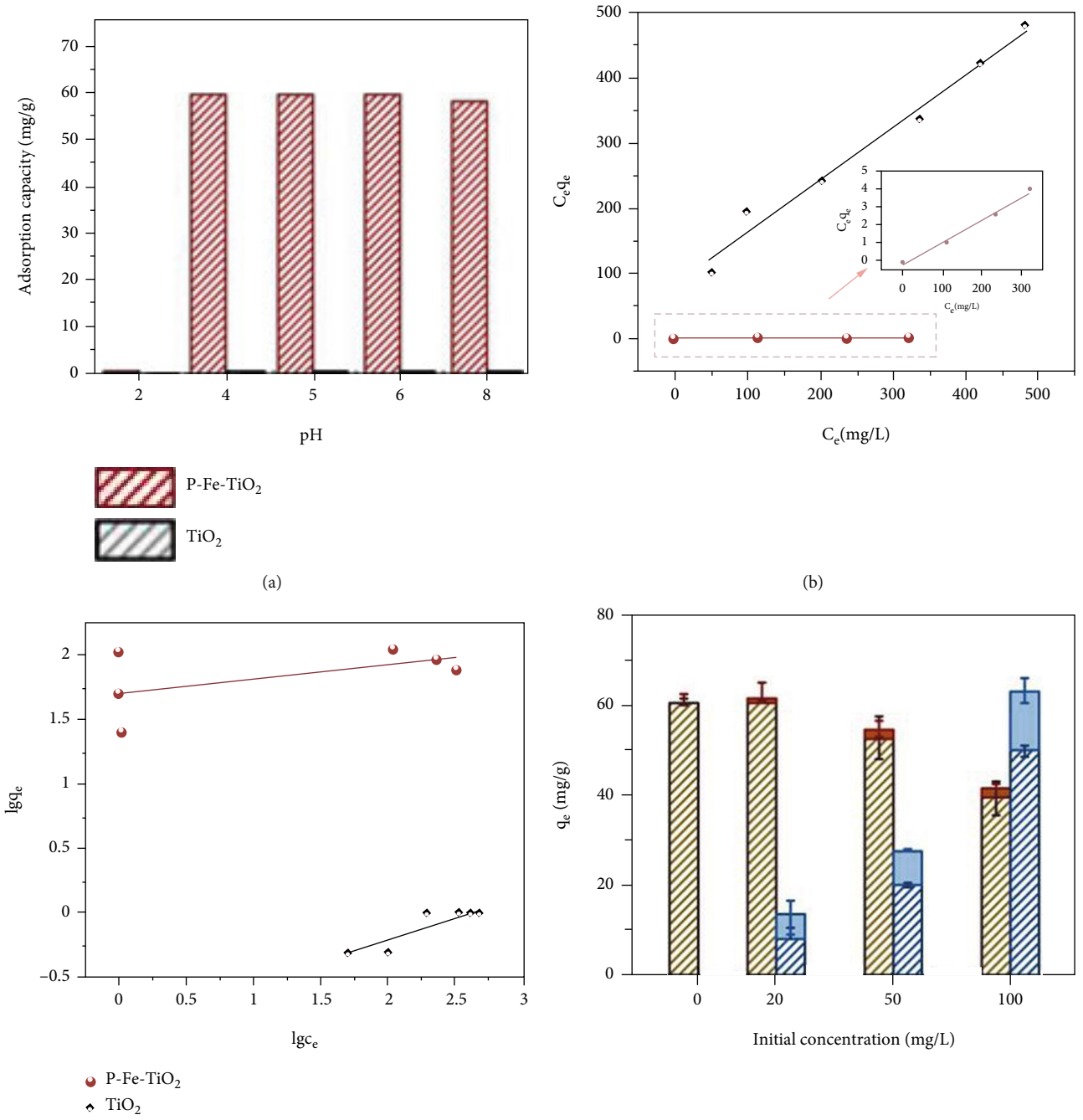

Figure 4: Continued.

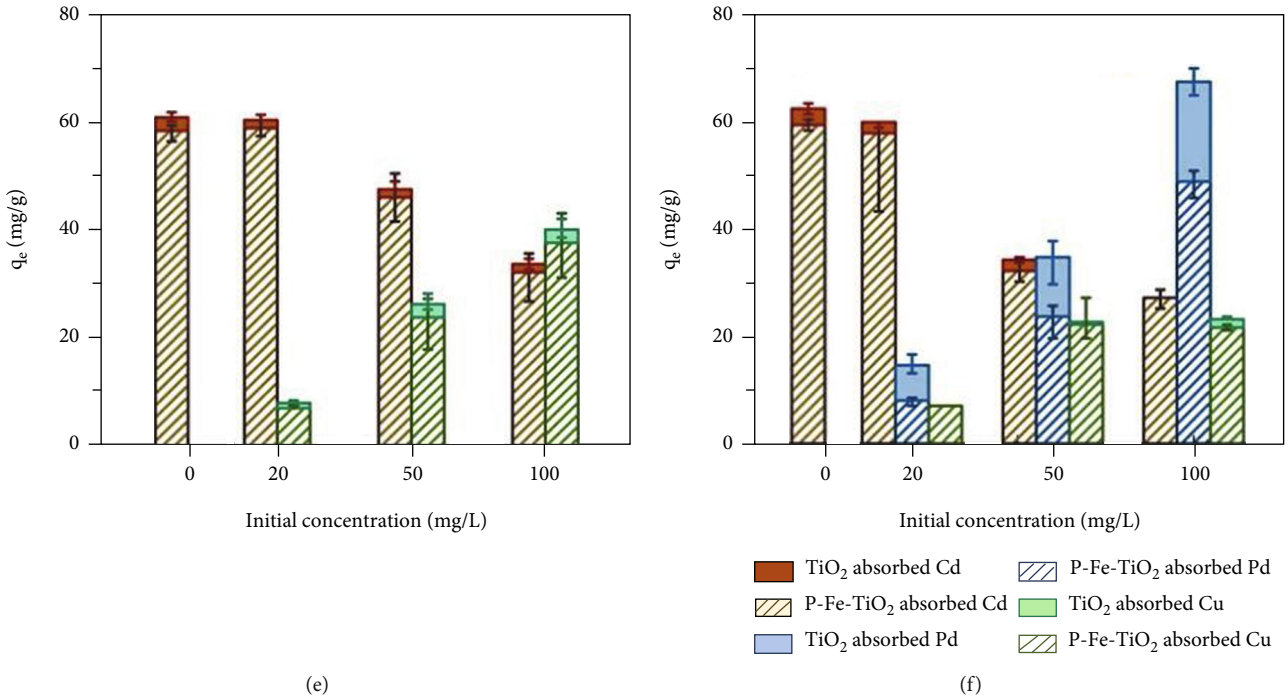

Figure 4: (a) Effects of pH; (b) Langmuir adsorption isotherm model; (c) Freundlich adsorption isotherm model; (d) influence of Pb(II) competitive adsorption; (e) influence of Cu(II) competitive adsorption; (f) effect of Pb(II) and Cu(II) competitive coadsorption.

Table 1: Parameters of adsorption isotherm models.

Sample	Langmuir model			Freundlich model		
	q_{max} (mg/g)	K_L (L/mg)	R^2	K_F ($mg^{1-n}L^n/g$)	n	R^2
P-Fe-TiO_2	83.33	-0.15	0.985	50.93	8.90	0.338
TiO_2	1.24	0.01	0.978	0.12	2.75	0.828

also promotes the action of electrostatic attraction, as shown in the SEM and BET characterization analysis above. The kinetic fitting analysis results at different temperatures show that the adsorption capacity of the modified material is affected by temperature, so we further analyzed and investigated the thermodynamic properties; the analysis results that initial concentration is 400 mg/L are shown in Table 3. From the data in Table 3, ΔG is negative, which indicates that the adsorption process of P-Fe-TiO_2 on Cd(II) is spontaneous, and the value of ΔG decreases with increasing temperature. This result shows that increasing temperature is beneficial to the adsorption process. A positive value of ΔH indicates that the adsorption process is endothermic. A positive value of ΔS indicates an increase in entropy during the adsorption process, indicating an increase in the disorder of the adsorption system [45]. To further explore the adsorption mechanism of P-Fe-TiO_2 for Cd(II), as well as the observed competitive adsorption effect of Pb(II) and Cu(II) on Cd(II), we used DFT calculations to verify the experimental results.

3.6. DFT Calculations

3.6.1. Binding Energy and HOMO LUMO (FMO) Analysis. The binding energies of Cd(II) with TiO_2 and of P-Fe-TiO_2 with Cd(II), Pb(II), and Cu(II) are shown in Table 4. From the table, binding energy is positively correlated with the absolute value of $E_{(ab)}$. The larger the absolute value of $E_{(ab)}$ is, the stronger the binding between the adsorbate and the adsorbent [27, 46]. The binding energy of TiO_2 for Cd(II) is almost just half than that of the modified material (P-Fe-TiO_2), so P-Fe-TiO_2 exhibits improved adsorption of Cd(II) owing to its modification with a combination of a metal, a nonmetal, and associated functional groups, which greatly improves the binding energy between the adsorbent and the heavy metal. In addition, the binding capacity of P-Fe-TiO_2 for Pb(II) is the strongest, followed by that for Cd(II), and the weakest binding capacity is that for Cu(II), which is in line with the results of the competitive adsorption experiment (Figure 4(f)). To further study the differences in adsorption among different heavy metals, we performed calculation fitting analysis on the HOMO and LUMO of Cd(II), Pb(II), and Cu(II) with P-Fe-TiO_2, as shown in Figure 6. The HOMO energy indicates the ability to contribute electrons, and the LUMO energy indicates the ability to accept electrons; the HOMO and LUMO, frontier molecular orbitals (FMOs), can determine the direct binding mode of adsorbents and adsorbed heavy metals and indicate stability and reactivity [47]. As seen from the

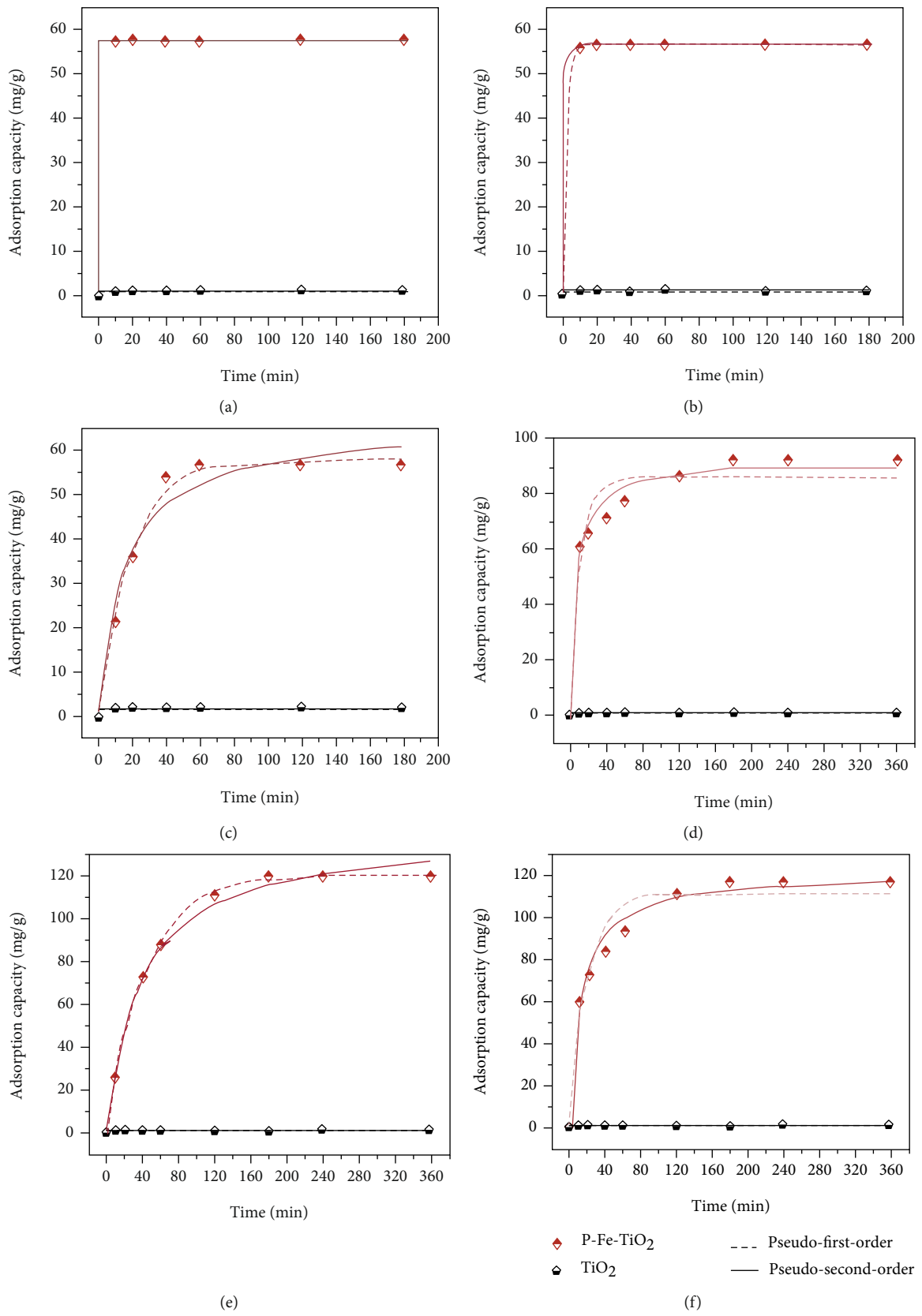

Figure 5: Fitting of pseudo-first-order kinetic and pseudo-second-order kinetic models to TiO_2 and P-Fe-TiO_2 data at (a) 10°C, (b) 25°C, and (c) 40°C with the initial concentration of 100 mg/L and at (d) 10°C, (e) 25°C, and (f) 40°C with the initial concentration of 400 mg/L.

Table 2: Kinetic parameters of P-Fe-TiO_2 and TiO_2 at different temperatures and initial concentrations.

		10°C			25°C			40°C		
		Pseudo-first-order kinetics								
100 mg/L	Sample	q_{e1}	K_1	R_1^2	q_{e1}	K_1	R_1^2	q_{e1}	K_1	R_1^2
	P-Fe-TiO_2	57.5	$1.32\,E^{14}$	1	56.9	0.179	0.999	59.4	0.022	0.992
	TiO_2	1	1.663	1	1	1.663	1	1	1.663	1
		Pseudo-second-order kinetics								
		q_{e2}	K_2	R_2^2	q_{e2}	K_2	R_2^2	q_{e2}	K_2	R_2^2
	P-Fe-TiO_2	57.5	$1.53\,E^{11}$	1	57.1	0.086	0.999	67.3	0.181	0.966
	TiO_2	1	$2.48\,E^{12}$	1	1	$6.19\,E^{12}$	1	1	$1.92\,E^{12}$	1
		Pseudo-first-order kinetics								
400 mg/L	Sample	q_{e1}	K_1	R_1^2	q_{e1}	K_1	R_1^2	q_{e1}	K_1	R_1^2
	P-Fe-TiO_2	92.5	0.049	0.945	119.5	0.010	0.998	121	0.026	0.940
	TiO_2	1	1.663	1	1	1.663	1	1	1.663	1
		Pseudo-second-order kinetics								
		q_{e2}	K_2	R_2^2	q_{e2}	K_2	R_2^2	q_{e2}	K_2	R_2^2
	P-Fe-TiO_2	92.5	0.002	0.979	119.5	0.026	0.998	121	0.117	0.981
	TiO_2	1	$8.15\,E^{11}$	1	1	$2.11\,E^{12}$	1	1	$8.15\,E^{11}$	1

Table 3: Adsorption thermodynamic parameters of Cd(II) on P-Fe-TiO_2 at 400 mg/L of initial concentrations.

T (K)	ΔG (kJ·mol^{-1})	ΔH (kJ·mol^{-1})	ΔS (J·mol^{-1}·K^{-1})
283	-0.38		
298	-0.92	13.09	47.56
313	-1.62		

Table 4: Binding energies of Cd(II) with a single adsorbent and the binding energy of P-TiO_2 with Cd(II), Pb(II), and Cu(II).

Samples	$E_{(a)}$ (Ha)	$E_{(b)}$ (Ha)	$E_{(ab)}$ (Ha)	BE (kcal/mol)
TiO_2+Cd	-999.75	-5466.58	-6466.63	62.75
P-Fe-TiO_2+Cd	-2982.54	-5466.58	-8449.25	81.58
P-Fe-TiO_2+Pb	-2982.54	-19527.41	-22510.18	144.33
P-Fe-TiO_2+Cu	-2982.54	-1639.73	-4622.38	69.03

figure, the LUMO of P-Fe-TiO_2 in P-Fe-TiO_2-Cd and P-Fe-TiO_2-Cu is transferred to Cd(II) and Cu(II), and some of the HOMOs of P-Fe-TiO_2 in P-Fe-TiO_2-Pb and P-Fe-TiO_2-Cu are transferred to Pb(II) and Cu(II), which shows that there is charge transfer between the three heavy metal ions and P-Fe-TiO_2. This finding is in agreement with the experimental results, in which Pb(II) and Cu(II) have a great influence on the adsorption process of Cd(II). A chemical adsorption effect clearly exists in the adsorption of Cd(II), which also shows that the kinetic results match the pseudo-second-order kinetic equation best. P-Fe-TiO_2-Cd, P-Fe-TiO_2-Pb, and P-Fe-TiO_2-Cd have a smaller energy gap between the HOMO and LUMO than does P-Fe-TiO_2. A smaller energy gap indicates that the corresponding conjugate is more stable [48], which shows that the structure of P-Fe-TiO_2 is more stable after being combined with heavy metal ions. In addition, the Mulliken charge analysis proved that the best binding site for heavy metal ions is the O atom bridging P and Fe because it has the strongest negative charge (i.e., the O atom with a -0.791C charge in Figure 7(b), the O atom with a -0.772C charge in Figure 7(c), and the O atom with a -0.757C charge in Figure 7(d)) and has the greatest attraction to heavy metal ions (Zhang and Zheng et al., 2021b), as shown in Figure 7. The surrounding negatively charged oxygen atoms also have a certain binding effect, as also confirmed by the FTIR and XPS analyses. The adsorption of Cd(II) by P-Fe-TiO_2 is greatly influenced by P-O, P=O, Fe-O, and -OH groups.

3.6.2. MEP Analysis. Molecular electrostatic potential (MEP) analysis plays an important role in finding the reaction sites of adsorbents and adsorbed heavy metals and judging the nucleophilicity (positive charge) and electrophilicity (negative charge) of electron positions [49, 50]. The MEP analysis of P-Fe-TiO_2, P-Fe-TiO_2-Cd, P-Fe-TiO_2-Pb, and P-Fe-TiO_2-Cu is shown in Figure 8. In the figure, blue regions represent the MEP positions with the largest positive values, and red regions represent the MEP positions with the smallest negative values [51]. From the figure, the red areas are essentially concentrated near the groups containing Fe and P, indicating that these areas are more electrophilic. Therefore, positively charged Cd(II), Pb(II), and Cu(II) are more likely to be attracted by the charges at these sites. This finding is also consistent with the Mulliken and FMO analytical results. In the binding energy analysis, the binding energy of P-Fe-TiO_2-Pb is the largest, followed by P-Fe-TiO_2-Cd, and P-Fe-TiO_2-Cu is the smallest. In the MEP diagram (Figure 8), P-Fe-TiO_2-Cu has the smallest color difference between red and blue, and the image of P-Fe-TiO_2-Pb and

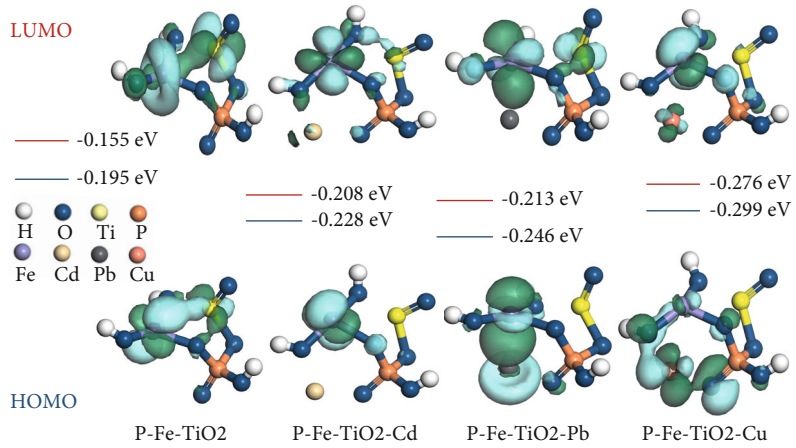

Figure 6: Orbital diagrams of the HOMOs and LUMOs of P-Fe-TiO_2, P-Fe-TiO_2-Cd, P-Fe-TiO_2-Pb, and P-Fe-TiO_2-Cu.

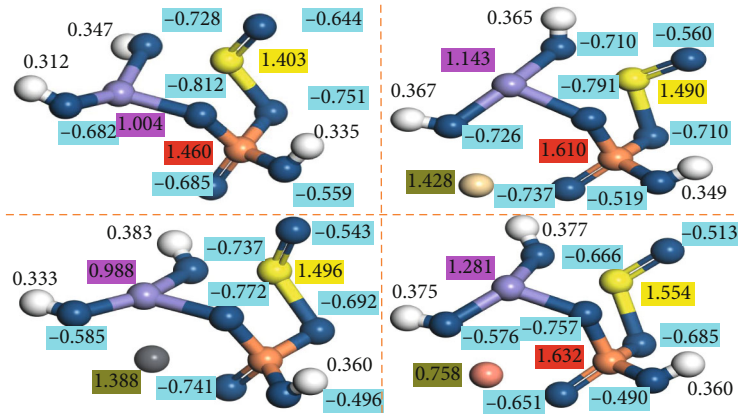

Figure 7: Mulliken charge population analysis of (a) P-Fe-TiO_2, (b) P-Fe-TiO_2-Cd, (c) P-Fe-TiO_2-Pb, and (d) P-Fe-TiO_2-Cu.

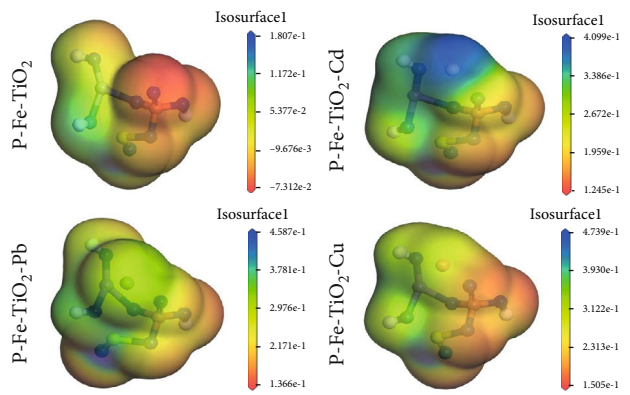

Figure 8: MEP images of P-Fe-TiO_2, P-Fe-TiO_2-Cd, P-Fe-TiO_2-Pb, and P-Fe-TiO_2-Cu.

P-Fe-TiO_2-Cd can see the obvious difference between blue and red. It shows that the distinction between positive and negative charges is more obvious, so the binding effect is stronger, which is consistent with the experimental results. A comparison of the MEP diagrams before and after the adsorption of Cd(II), Pb(II), and Cu(II) shows that the addition of heavy metal ions increases the positivity of P-Fe-TiO_2, indicating that P-Fe-TiO_2 is affected by electrostatic effects on Cd(II), Pb(II), and Cu(II).

3.6.3. Total Electron Density and Differential Charge Analysis. The previous analysis shows that electron sharing or electron exchange is involved in the adsorption process. Therefore, the adsorption mechanism at the electron level was further studied through the calculation and analysis of the total electron density and the differential charge. The total electron density map and the differential charge map of P-Fe-TiO_2 and various metal ions are shown in Figure 9. The figure shows the degree of electron cloud overlap between P-Fe-TiO_2 and heavy metal ions and the degree of their binding ability. As the color changes from blue to red, the charge density continues to increase and the binding ability continues to strengthen [52]. The differential charge shows the donation (red part) and acceptance (blue part) of charge between P-Fe-TiO_2 and heavy metal ions [53]. From Figures 9(a), 9(c), 9(e), and 9(g), it can be seen that the degree of coincidence between the electron clouds of Pb(II) and P-Fe-TiO_2 is higher than that of Cd(II) and Cu(II). Therefore, the affinity of Pb(II) to P-Fe-TiO_2 is the strongest and that of Cu(II) is the weakest [53]. The results

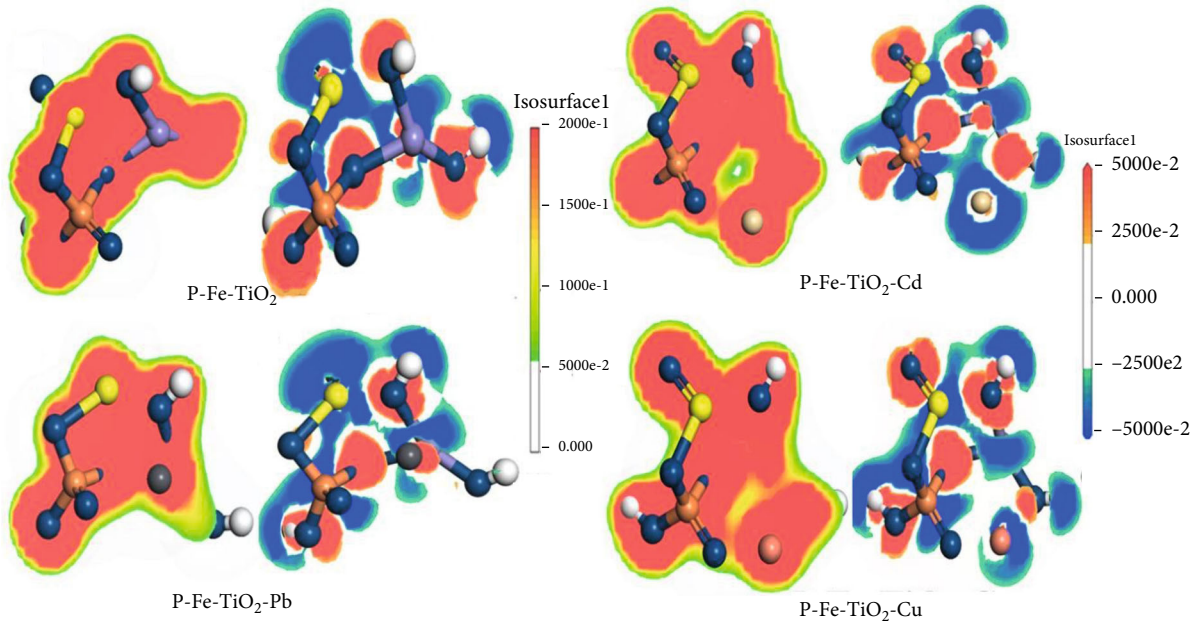

FIGURE 9: Analysis of total electron density and differential charge for P-Fe-TiO_2, P-Fe-TiO_2-Cd, P-Fe-TiO_2-Pb, and P-Fe-TiO_2-Cu; (a, c, e, g) the total electron density; (b, d, f, h) the differential charge; (1) is the color legend for total electron density, and (2) is the color legend for differential charge.

are consistent with the results of FMO and MEP analysis. The above relationship can also be explained by differential charge simulation images (Figures 9(b), 9(e), and 9(h)). Compared with Cd(II) and Cu(II), Pb(II) has a stronger electron capacity, and more Pb(II) than Cu(II) is adsorbed in competitive adsorption.

4. Conclusion

In summary, we used KH_2PO_4 and $FeCl_3$ to successfully modify TiO_2 with metal and nonmetal composites and introduced P-O, P=O, Fe-O, and -OH groups. The experimental adsorption kinetic results show that the adsorption process of P-Fe-TiO_2 for Cd(II) is mainly controlled by chemical adsorption and physical adsorption, and the maximum adsorption capacity can reach 121 mg/g. In the competitive adsorption experiment, both Pb(II) and Cu(II) affected the adsorption of Cd(II). The adsorption order of P-Fe-TiO_2 for the three heavy metal ions is Pb(II) > Cd(II) > Cu(II), as also confirmed by DFT calculations. The binding energy and FMO analyses show that electron transfer occurs between the adsorbent and heavy metal ions and a chemical reaction takes place. The results of Mulliken, electrostatic potential, total potential, and differential charge analysis, including the adsorbent sites, binding sites, and binding strengths of Cd(II), Pb(II), and Cu(II), further proved the experimentally observed difference in competitive adsorption.

Data Availability

The data used to support the findings of this study are included within the article.

Conflicts of Interest

The authors declare no competing financial interest.

Acknowledgments

The authors acknowledge funding from Key-Area Research and Development Program of Guangdong Province (2019B110207001), Guangzhou Municipal Science and Technology Project (201803030001), Natural Science Foundation of Guangdong Province (2018A030313363), National Natural Science Foundation of China (No. 51508206), and Guangdong Provincial Key Laboratory of Chemical Pollution and Environmental Safety (2019B030301008).

References

[1] G. J. Joshiba, P. S. Kumar, M. Govarthanan, P. T. Ngueagni, A. Abilarasu, and F. Carolin C, "Investigation of magnetic silica nanocomposite immobilized *Pseudomonas fluorescens* as a biosorbent for the effective sequestration of Rhodamine B from aqueous systems," *Environmental Pollution*, vol. 269, 2021.

[2] M. Sridevi, C. Nirmala, N. Jawahar, G. Arthi, S. Vallinayagam, and V. K. Sharma, "Role of nanomaterial's as adsorbent for heterogeneous reaction in waste water treatment," *Journal of Molecular Structure*, vol. 1241, 2021.

[3] Y. Zou, X. Wang, A. Khan et al., "Environmental remediation and application of nanoscale zero-valent iron and its composites for the removal of heavy metal ions: a review," *Environmental Science & Technology*, vol. 50, no. 14, pp. 7290–7304, 2016.

[4] Z. Sun, Y. Liu, and C. Srinivasakannan, "One-pot fabrication of rod-like magnesium silicate and its adsorption for Cd^{2+},"

Journal of Environmental Chemical Engineering, vol. 8, no. 5, 2020.

[5] F. Wang, M. Hao, J. Liang et al., "A facile fabrication of sepiolite mineral nanofibers with excellent adsorption performance for Cd^{2+} ions," *RSC Advances*, vol. 9, no. 69, pp. 40184–40189, 2019.

[6] Z. Zhu, Z. Chen, X. Luo, W. Zhang, and S. Meng, "Gravity-driven biomimetic membrane (GDBM): an ecological water treatment technology for water purification in the open natural water system," *Chemical Engineering Journal*, vol. 399, 2020.

[7] F. L. Souza, M. Zougagh, C. Sáez, P. Cañizares, A. Ríos, and M. A. Rodrigo, "Electrochemically-based hybrid oxidative technologies for the treatment of micropollutants in drinking water," *Chemical Engineering Journal*, vol. 414, 2021.

[8] I. Ali, A. A. Basheer, X. Y. Mbianda et al., "Graphene based adsorbents for remediation of noxious pollutants from wastewater," *Environment International*, vol. 127, pp. 160–180, 2019.

[9] M. Hassan, R. Naidu, J. Du, Y. Liu, and F. Qi, "Critical review of magnetic biosorbents: their preparation, application, and regeneration for wastewater treatment," *Science of The Total Environment*, vol. 702, 2020.

[10] B. Sun, W. Zhou, H. Li et al., "Synthesis of particulate hierarchical tandem heterojunctions toward optimized photocatalytic hydrogen production," *Advanced Materials*, vol. 30, no. 43, 2018.

[11] Y. Zhang, C. Han, G. Zhang, D. D. Dionysiou, and M. N. Nadagouda, "PEG-assisted synthesis of crystal TiO_2 nanowires with high specific surface area for enhanced photocatalytic degradation of atrazine," *Chemical Engineering Journal*, vol. 268, pp. 170–179, 2015.

[12] J. Cui, J. Du, S. Yu, C. Jing, and T. Chan, "Groundwater arsenic removal using granular TiO_2: integrated laboratory and field study," *Environmental Science and Pollution Research International*, vol. 22, no. 11, pp. 8224–8234, 2015.

[13] J. Hu and H. J. Shipley, "Regeneration of spent TiO_2 nanoparticles for Pb (II), Cu (II), and Zn (II) removal," *Environmental Science and Pollution Research International*, vol. 20, no. 8, pp. 5125–5137, 2013.

[14] S. Hu, L. Yan, T. Chan, and C. Jing, "Molecular insights into ternary surface complexation of arsenite and cadmium on TiO_2," *Environmental Science & Technology*, vol. 49, no. 10, pp. 5973–5979, 2015.

[15] N. Wu, H. Wei, and L. Zhang, "Efficient removal of heavy metal ions with biopolymer template synthesized mesoporous titania beads of hundreds of micrometers size," *Environmental Science & Technology*, vol. 46, no. 1, pp. 419–425, 2012.

[16] T. Wang, W. Liu, L. Xiong, N. Xu, and J. Ni, "Influence of pH, ionic strength and humic acid on competitive adsorption of Pb(II), Cd(II) and Cr(III) onto titanate nanotubes," *Chemical Engineering Journal*, vol. 215-216, pp. 366–374, 2013.

[17] W. Liu, T. Wang, A. G. Borthwick et al., "Adsorption of Pb^{2+}, Cd^{2+}, Cu^{2+} and Cr^{3+} onto titanate nanotubes: Competition and effect of inorganic ions," *Science of The Total Environment*, vol. 456-457, pp. 171–180, 2013.

[18] Y. Zhang, Y. Zhang, Y. Huang et al., "Adsorptive-photocatalytic performance and mechanism of Me (Mn,Fe)-N co-doped TiO_2/SiO_2 in cyanide wastewater," *Journal of Alloys and Compounds*, vol. 867, 2021.

[19] W. Peng, S. Du, Z. Shaoning et al., "Constructing mesoporous phosphated titanium oxide for efficient Cr(III) removal," *Journal of Hazardous Materials*, vol. 384, 2020.

[20] K. L. Tan and B. H. Hameed, "Insight into the adsorption kinetics models for the removal of contaminants from aqueous solutions," *Journal of the Taiwan Institute of Chemical Engineers*, vol. 74, pp. 25–48, 2017.

[21] L. Zheng, C. Wang, Y. Shu, X. Yan, and L. Li, "Utilization of diatomite/chitosan-Fe (III) composite for the removal of anionic azo dyes from wastewater: Equilibrium, kinetics and thermodynamics," *Colloids and Surfaces A: Physicochemical and Engineering Aspects*, vol. 468, pp. 129–139, 2015.

[22] J. Wang and X. Guo, "Adsorption kinetic models: physical meanings, applications, and solving methods," *Journal of Hazardous Materials*, vol. 390, 2020.

[23] S. Zhuang and J. Wang, "Removal of cobalt ion from aqueous solution using magnetic graphene oxide/chitosan composite," *Environmental Progress & Sustainable Energy*, vol. 38, no. s1, pp. S32–S41, 2019.

[24] J. O. Ighalo and A. G. Adeniyi, "A mini-review of the morphological properties of biosorbents derived from plant leaves," *SN Applied Sciences*, vol. 2, no. 3, 2020.

[25] J. Zhang, Z. Yan, L. Fu et al., "Silver nanoparticles assembled on modified sepiolite nanofibers for enhanced catalytic reduction of 4-nitrophenol," *Applied Clay Science*, vol. 166, pp. 166–173, 2018.

[26] Y.-X. Li, C.-C. Wang, H. Fu, and P. Wang, "Marigold-flower-like TiO_2/MIL-125 core–shell composite for enhanced photocatalytic Cr(VI) reduction," *Journal of Environmental Chemical Engineering*, vol. 9, no. 4, 2021.

[27] L. Zheng, D. Peng, S. Zhang, Y. Yang, L. Zhang, and P. Meng, "Adsorption of sulfamethoxazole and sulfadiazine on phosphorus-containing stalk cellulose under different water pH studied by quantitative evaluation," *Environmental Science and Pollution Research International*, vol. 27, no. 34, pp. 43246–43261, 2020.

[28] A. J. Kinfack Leoga, L. Youssef, S. Roualdès, and V. Rouessac, "Phosphonic acid-based membranes as proton conductors prepared by a pulsed plasma enhanced chemical vapor deposition technique," *Thin Solid Films*, vol. 660, pp. 506–515, 2018.

[29] X. Fan, T. Yu, Y. Wang et al., "Role of phosphorus in synthesis of phosphated mesoporous TiO_2 photocatalytic materials by EISA method," *Applied Surface Science*, vol. 254, no. 16, pp. 5191–5198, 2008.

[30] R. Quiñones, S. Garretson, G. Behnke et al., "Fabrication of phosphonic acid films on nitinol nanoparticles by dynamic covalent assembly," *Thin Solid Films*, vol. 642, pp. 195–206, 2017.

[31] S. Yu, L. Zhai, S. Zhong, Y. Qiu, L. Cheng, and X. Ren, "Synthesis and structural characterization of magnetite/sepiolite composite and its sorptive properties for Co(II) and Cd(II)," *Journal of the Taiwan Institute of Chemical Engineers*, vol. 59, pp. 221–228, 2016.

[32] A. Ahmed, A. Singh, A. Sharma et al., "Investigating the thermographical effect on optical properties of Eu doped Y_2O_3:TiO_2 nanocomposite synthesized via sol-gel method," *Solid State Sciences*, vol. 116, 2021.

[33] Z. Wang, A. Mahmood, X. Xie, X. Wang, H. Qiu, and J. Sun, "Surface adsorption configurations of H_3PO_4 modified TiO_2 and its influence on the photodegradation intermediates of

gaseous o-xylene," *Chemical Engineering Journal*, vol. 393, 2020.

[34] H. Fei, X. Zhou, H. Zhou et al., "Facile template-free synthesis of meso-macroporous titanium phosphate with hierarchical pore structure," *Microporous and Mesoporous Materials*, vol. 100, no. 1-3, pp. 139–145, 2007.

[35] A. J. Habish, S. Lazarević, I. Janković-Častvan et al., "Nanoscale zerovalent iron (nZVI) supported by natural and acid-activated sepiolites: the effect of the nZVI/support ratio on the composite properties and $^{Cd2+}$ adsorption," *Environmental Science and Pollution Research International*, vol. 24, no. 1, pp. 628–643, 2017.

[36] S. Zhuang and J. Wang, "Removal of U(VI) from aqueous solution using phosphate functionalized bacterial cellulose as efficient adsorbent," *Radiochimica Acta*, vol. 107, no. 6, pp. 459–467, 2019.

[37] T. Zhang, L. Zheng, H. Yu et al., "Solution pH affects single, sequential and binary systems of sulfamethoxazole and cadmium adsorption by self-assembled cellulose: promotion or inhibition?," *Journal of Hazardous Materials*, vol. 402, 2021.

[38] N. Yao, C. Li, J. Yu et al., "Insight into adsorption of combined antibiotic-heavy metal contaminants on graphene oxide in water," *Separation and Purification Technology*, vol. 236, 2020.

[39] H. Yu, L. Zheng, T. Zhang et al., "Adsorption behavior of Cd (II) on TEMPO-oxidized cellulose in inorganic/ organic complex systems," *Environmental Research*, vol. 195, 2021.

[40] L. Zheng, D. Peng, and P. Meng, "Promotion effects of nitrogenous and oxygenic functional groups on cadmium (II) removal by carboxylated corn stalk," *Journal of Cleaner Production*, vol. 201, pp. 609–623, 2018.

[41] L. Zheng, Y. Yang, P. Meng, and D. Peng, "Absorption of cadmium (II) via sulfur-chelating based cellulose: characterization, isotherm models and their error analysis," *Carbohydrate Polymers*, vol. 209, pp. 38–50, 2019.

[42] M. Basu, A. K. Guha, and L. Ray, "Adsorption behavior of cadmium on husk of lentil," *Process Safety and Environmental Protection*, vol. 106, pp. 11–22, 2017.

[43] Q. Kong, B. Xie, S. Preis, Y. Hu, H. Wu, and C. Wei, "Adsorption of Cd^{2+} by an ion-imprinted thiol-functionalized polymer in competition with heavy metal ions and organic acids," *RSC Advances*, vol. 8, no. 16, pp. 8950–8960, 2018.

[44] J. Liang, X. Li, Z. Yu et al., "Amorphous MnO2Modified biochar derived from aerobically composted swine manure for adsorption of Pb(II) and Cd(II)," *ACS Sustainable Chemistry & Engineering*, vol. 5, no. 6, pp. 5049–5058, 2017.

[45] L. Zheng, Z. Dang, X. Yi, and H. Zhang, "Equilibrium and kinetic studies of adsorption of Cd(II) from aqueous solution using modified corn stalk," *Journal of Hazardous Materials*, vol. 176, no. 1-3, pp. 650–656, 2010.

[46] L. Zheng, S. Zhang, W. Cheng et al., "Theoretical calculations, molecular dynamics simulations and experimental investigation of the adsorption of cadmium(ii) on amidoxime-chelating cellulose," *Journal of Materials Chemistry A*, vol. 7, no. 22, pp. 13714–13726, 2019.

[47] M. Feizi-Dehnayebi, E. Dehghanian, and H. Mansouri-Torshizi, "Synthesis and characterization of Pd(II) antitumor complex, DFT calculation and DNA/BSA binding insight through the combined experimental and theoretical aspects," *Journal of Molecular Structure*, vol. 1240, 2021.

[48] N. A. S. Pungut, M. P. Heng, H. M. Saad, K. S. Sim, V. S. Lee, and K. W. Tan, "From one to three, modifications of sensing behavior with solvent system: DFT calculations and real-life application in detection of multianalytes (Cu^{2+}, Ni^{2+} and Co^{2+}) based on a colorimetric Schiff base probe," *Journal of Molecular Structure*, vol. 1238, 2021.

[49] M. R. Hossain, M. M. Hasan, N.-E. Ashrafi et al., "Adsorption behaviour of metronidazole drug molecule on the surface of hydrogenated graphene, boron nitride and boron carbide nanosheets in gaseous and aqueous medium: a comparative DFT and QTAIM insight," *Physica E: Low-dimensional Systems and Nanostructures*, vol. 126, 2021.

[50] A. Nakhli, M. Bergaoui, K. H. Toumi et al., "Molecular insights through computational modeling of methylene blue adsorption onto low-cost adsorbents derived from natural materials: A multi-model's approach," *Computers & Chemical Engineering*, vol. 140, 2020.

[51] T. Zhang, L. Zheng, H. Yu et al., "Multiple adsorption systems and electron-scale insights into the high efficiency coadsorption of a novel assembled cellulose via experiments and DFT calculations," *Journal of Hazardous Materials*, vol. 416, 2021.

[52] Q. Chen, J. Zheng, L. Zheng, Z. Dang, and L. Zhang, "Classical theory and electron-scale view of exceptional Cd(II) adsorption onto mesoporous cellulose biochar *via* experimental analysis coupled with DFT calculations," *Chemical Engineering Journal*, vol. 350, pp. 1000–1009, 2018.

[53] Q. Chen, X. Wang, P. Yi et al., "Key roles of electron cloud density and configuration in the adsorption of sulfonamide antibiotics on carbonaceous materials: molecular dynamics and quantum chemical investigations," *Applied Surface Science*, vol. 536, 2021.